Journal of
Mechanics of
Materials and Structures

TWO-DIMENSIONAL SHOCK INDUCED COLLAPSE OF GAS BUBBLE NEAR A SEMIINFINITE DEFORMABLE SOLID

Wenfeng Xie and Yin Lu Young

Volume 2, Nº 10 December 2007

mathematical sciences publishers

JOURNAL OF MECHANICS OF MATERIALS AND STRUCTURES
Vol. 2, No. 10, 2007

TWO-DIMENSIONAL SHOCK INDUCED COLLAPSE OF GAS BUBBLE NEAR A SEMIINFINITE DEFORMABLE SOLID

WENFENG XIE AND YIN LU YOUNG

In this paper, the effect of shock-induced collapse of a single gas bubble on the transient fluid and solid response is numerically investigated. The jet-like bubble collapse and subsequent strong pressure loading on a nearby semiinfinite deformable solid structure are captured and simulated using a multiphase compressible hydrodynamic model. The objective is to understand the fluid-structure interaction mechanisms, including the effect of the compressibility of the solid medium on the bubble dynamics and shock wave propagation, and the effect of shock wave propagation on the transient stress distribution within the solid. Numerical results demonstrate that the bubble collapse can impart very high pressure pulses to the nearby structure, leading to very high stresses sustained by the solid. The solid can experience significant deformation, including yielding, depending on the local fluid conditions.

1. Introduction

Cavitation bubble collapse near a solid boundary can be found in many fields of engineering. Settings include marine (propellers, torpedoes, and ships) and civil structures (dams and spillways). In addition, cavitation bubble dynamics can be relevant to many biomedical applications including shock wave lithotripsy, drug delivery, and other high intensity ultrasonic therapies [Zhong et al. 1997; Ohl and Irink 2003; Ohl and Wolfrum 2003]. Shock-induced collapse of gas bubbles near solid boundaries exhibits very complex dynamics involving nonspherical bubbles, jet formation, jet impact on structure, jet-induced shock-structure interaction, and subsequent structural deformation.

A number of theoretical and experimental studies have explored cavitation bubble dynamics near solid boundaries [Knapp et al. 1970; Tomita and Shima 1986; Philipp and Lauterborn 1998; Tomita et al. 2002]. It has been found that the bubble is no longer spherically symmetric during collapse near a solid boundary. A liquid jet develops on the side of the bubble opposite the boundary and travels toward the boundary. The bubble collapses when the liquid jet penetrates the side of the bubble facing the boundary [Lindau and Lauterborn 2003]. Subsequently, a high velocity jet and strong pressure pulses are directed toward the solid, which can severely erode it.

It is important to know when a structure will deform or even fail under strong pressure. Earlier numerical studies on elastic structural response of air/underwater shock loads can be found in [Houlston et al. 1985; McCoy and Sun 1997], where the dynamic response of isotropic materials subject to blast loading was modeled using finite element method (FEM). Recently, analytical modeling and numerical

Keywords: bubble collapse, multiphase model, fluid-structure interaction, shock-bubble interaction.
The authors are grateful to the Office of Naval Research for their financial support through Grant no. N00014-05-1-0694, and the National Science Foundation through Grant no. 0530759.

analysis have been conducted to investigate the shock response of sandwich plates subjected to underwater blast loading [Xue and Hutchinson 2004; Deshpande and Fleck 2005; Deshpande et al. 2006]. They represented pressure loads by the acoustic approximation but did not account for the nonlinearity of fluid compressibility. To overcome this difficulty, [Kambouchev et al. 2006] extended Taylor's analysis to include nonlinear compressibility effects of the fluid medium and developed a numerical method based on the Lagrangian formulation of the compressible Eulerian equations. This method has been tested against various blast intensities and was recently employed to study metal sandwich plates subjected to intense air shocks [Vaziri and Hutchinson 2007]. It should be noted that Kambouchev et al. [2006] focused on the dynamic response of the rigid plates and assumed that the plate deformation and stress-wave propagation through the plate are negligible. This assumption is valid for stiff materials like steel or copper but may not be for softer ones like aluminum and plastic, where significant energy dissipates through the fluid-solid interface and the stress-wave propagation becomes important [Xie et al. 2007b; Xie et al. 2006].

In most fluid-structure interaction models involving underwater explosions or cavitation collapse, the fluid pressure loads are imposed as boundary conditions for the solid model which calculates the structural response, and the fluid and structure models are not fully coupled. However, the structural motion and deformation can have a significant countereffect on the fluid. Therefore, full coupling between the fluid and structural solvers is important for practical applications. Kalumuck et al. [1995] and Chahine et al. [2003] simulated a loosely-coupled fluid-structure interaction (FSI) using a BEM-FEM coupled numerical scheme, examining interactions between a fluid and either rigid or deformable structures. Both papers ignored fluid compressibility and assumed a potential flow, which are common assumptions in the study of bubble dynamics. However, the potential flow assumption is actually not valid for fluid simulations having shock waves where the effect of fluid and/or air compressibility is significant.

During the shock-induced collapse of a gas bubble near a solid boundary, the resulting bubble collapse is very violent due to strong shock impact, which can lead to severe damage of the solid boundary. Due to the strong short-duration pressure loads, the solid can be simulated as a compressible fluid medium governed by the hydro-elasto-plastic equation of state [Tang and Sotiropoulos 1999; Xie et al. 2006]. Therefore, the system can be treated as a gas-water-solid three-phase compressible system and can thus be solved using a multiphase compressible hydrodynamic solver [Xie et al. 2007b; Xie et al. 2006]. The objective of this paper is to investigate the effect of shock-induced bubble collapse on a nearby semiinfinite solid and the countereffect of solid deformation on the fluid and bubble dynamics and on the shock wave propagation. The stress distribution within the compressible solid is also presented and analyzed.

2. Numerical methodology

In this work, all mediums are assumed to be compressible and isotropic, and interactions between mediums are always considered in the multiphase hydrodynamic computations. Therefore, the numerical method must be able to capture moving material interfaces. Due to strong shock wave propagation and high density ratios between the fluid mediums, the numerical method should be high-order (at least second), high resolution, and robust. The present numerical method, called the multiphase compressible hydrodynamic model (MCHM), comprises a second-order Monotone Upstream-centered Scheme for

Conservation Laws (MUSCL)—developed by Van Leer [1974] for calculating the fluid variables of the region away from the interfaces—and an explicit characteristic method [Xie et al. 2007b] for calculating the variables (pressure, velocity and entropy) at the interfaces.

2.1. ***Governing equations for compressible flows.*** The governing equations used in the present study are the Navier-Stokes equations for compressible flows, where the effects of turbulence and surface tension at the interfaces are neglected. This is a typical and realistic assumption for simulating flows in cold water and under high pressure conditions where the effects of temperature changes, surface tension, and turbulence are very small compared to the mechanical driving force (pressure) of the system. The conservative form of the two-dimensional Navier-Stokes equations can be written as

$$\frac{\partial U}{\partial t}+\frac{\partial F(U)}{\partial x}+\frac{\partial G(U)}{\partial y}=\frac{\partial F_v(U)}{\partial x}+\frac{\partial G_v(U)}{\partial y}, \tag{2–1}$$

where

$$U=[\rho,\rho u,\rho v,E]^T,$$

$$F(U)=\left[\rho u,\rho u^2+p,\rho uv,(E+p)u\right]^T,$$

$$G(U)=\left[\rho v,\rho uv,\rho v^2+p,(E+p)v\right]^T,$$

$$F_v(U)=\left[0,\frac{2}{3}\mu(2u_x-v_y),\mu(u_y+v_x),\frac{2}{3}\mu(2u_x-v_y)u+\mu(u_y+v_x)v\right]^T,$$

$$G_v(U)=\left[0,\mu(u_y+v_y),\frac{2}{3}\mu(2v_y-u_x),\mu(u_y+v_x)u+\frac{2}{3}\mu(2v_y-u_x)v\right]^T.$$

Here ρ is the gas flow density, $p=p(e,\rho)$ is the pressure, u and v are the flow velocities in the x (horizontal) and y (vertical) directions. E is the total energy and is given as $E=\rho e+0.5\rho(u^2+v^2)$, where e is the internal energy per unit mass. μ is the dynamic viscosity of the fluid. To close the Navier-Stokes Equation (2–1), equations of state (EOS) are required to represent the constitutive behavior of each medium, that is, for the gas, water, and solid. The typical equations of state for gas and water are the perfect gas law and Tait's equation:

$$p=(\gamma_g-1)\rho e,$$
$$p=B(\rho/\rho_0)^{\gamma_l}-B+A,$$

where γ_g is the ratio of specific heat for gas and is set to be 1.4. p_0 and ρ_0 are 10^5 Pa and 1000 kg/m^3. B, A and γ_l are constants of Tait's EOS and are set to 3.31×10^8 Pa, 10^5 Pa, and 7.0.

The hydro-elasto-plastic (HEP) equation of state is used to describe the fluid-like constitutive material behavior of the solid when subject to short-duration, high-impact loads. The HEP equation of state can be derived by decomposing the total stress and strain into a mean hydrodynamic component and a deviator component [Tang and Sotiropoulos 1999; Xie et al. 2006]:

$$p=p_h(\rho)+\frac{4}{3}s(\rho_0,\tau_0,\rho). \tag{2–2}$$

Equation (2–2) assumes the material's ability to support a deviator stress s can be described by the longitudinal and bulk wave speeds, and isentropic loading and unloading behavior. $p_h(\rho)$ and $s(\rho_0, \tau_0, \rho)$ denote the mean (hydrostatic) stress and deviator stress (difference between the principal stresses in the longitudinal and transverse directions) in the solid, and can be expressed as follows:

$$\begin{aligned} p_h(\rho) &= \frac{m}{\beta}\left(\left(\frac{\rho}{\rho_a}\right)^{\beta} - 1\right) + p_a, \\ s &= \begin{cases} \tau, & |\tau| < Y/2, \\ Y\,\mathrm{sign}(\tau)/2, & |\tau| \geq Y/2, \end{cases} \end{aligned} \tag{2–3}$$

where $\partial_t \tau = G/\rho \partial_t \rho$. Also $m = E/[3(1-2\mu)]$, Y, $G = E/[2(1+\mu)]$, and β are the bulk modulus, the yield stress, the modulus of rigidity, and a model constant. E and μ are Young's modulus and Poisson's ratio. The values of these parameters can be found in Table 1. Note that the first of Equation (2–3) is equivalent to Murnaghan pressure-volume equation, while the second is the Von Mises yield criterion. For simple tension/compression, Equation (2–2) can be written as:

$$p = \begin{cases} p_h(\rho) + \dfrac{2}{3}Y, & \rho \geq \rho_2, \\ p_h(\rho) + \dfrac{4}{3}\left(G \ln \dfrac{\rho}{\rho_0} + \tau_0\right), & \rho_1 < \rho \leq \rho_2, \\ p_h(\rho) - \dfrac{2}{3}Y, & \rho < \rho_1, \end{cases} \tag{2–4}$$

where $\rho_1 = \rho_0 \exp(-(2\tau_0 + Y)/2G)$ and $\rho_2 = \rho_0 \exp(-(2\tau_0 - Y)/2G)$ represent the equivalent compression and tension yield densities corresponding to a strain-hardening material. p_a, ρ_a, ρ_0 and τ_0 are the reference pressure, reference density, initial density, and initial shear stress. To yield more insight into the structural response, the normalized solid deviator stress $(2s/Y)$ can be calculated to assess potential

Parameter	Value
p_a	1.0 bar
ρ_a	2700 kg/m^3
β	5.275
m	6.863×10^{10} Pa
G	5.224×10^{10} Pa
Y	2.70×10^{8} Pa
τ_0	0.0 Pa

Table 1. Material properties of aluminum represented by the hydro-elasto-elastic equation of state.

yielding of a compressible structure. The value of $2s/Y$ is between -1.0 and 1.0. If $2s/Y = 1.0$ or -1.0, the structure has reached the Von Mises yield criterion.

It should be noted that the HEP is only valid for short time intervals when a very strong shock load is suddenly imposed normal to a semiinfinite homogeneous, isotropic solid. The HEP is able to capture both elastic and plastic deformations. That is, the solid can be under plastic compression, plastic tension, or elastic deformation for $\rho \geq \rho_2$, $\rho \leq \rho_1$, and $\rho_1 \leq \rho \leq \rho_2$, respectively. It should be emphasized that the current HEP equation of state ignores the propagation of shear (s-type) waves, and assumes the pressure (p-type) waves to travel along the principal directions. Hence, it is restricted to the modeling of very strong shock loads acting normal to the solid surface over a very short duration. For more general loading scenarios, or far more complex material behaviors, the solid should be modeled using the actual stress-strain constitutive relationships.

2.2. ***Multiphase compressible hydrodynamic model.*** For simulating multiphase compressible flow, the main difficulty is capturing material interfaces, where calculating one fluid medium requires information from adjacent fluid mediums. Due to different equations of state across the interfaces, the direct calculation of nearby flow variables without additional techniques for treating interfaces would lead to numerical oscillations near the interfaces. Therefore, an efficient and robust interface treatment technique is necessary. The multiphase compressible hydrodynamic model (MCHM) employs an explicit characteristic method to calculate interface variables (pressure, velocity and entropy), which is simplified from the modified ghost fluid method (MGFM by Liu et al. [2003]) and has been validated with one-dimensional analytical solutions in [Xie et al. 2007b]. Formulation of the explicit characteristic method for two-dimensional problems starts from the characteristic equations for Equation (2–1) in the normal direction of the material interface:

$$\begin{aligned} &\frac{dp_I}{dt} + \rho_{IL} c_{IL} \frac{du_I}{dt} = 0, \qquad \text{along} \quad \frac{dx}{dt} = u_I + c_{IL}, \\ &\frac{dp_I}{dt} - \rho_{IR} c_{IR} \frac{du_I}{dt} = 0, \qquad \text{along} \quad \frac{dx}{dt} = u_I - c_{IR}. \end{aligned} \tag{2–5}$$

Here subscripts I, IL, and IR refer to the interface, the left side of the interface, and the right side of the interface; $\rho_{IL}(\rho_{IR})$ and $c_{IL}(c_{IR})$ are the density and sound speed at the left (right) side of the interface; u_I and p_I are the normal velocity and pressure at the interface. The spatial coordinates of the transient gas bubble interface and water-structure interface are tracked as zero levels of ϕ and ψ, two scalar level set indicator functions which can be solved using the transportation equation [Osher and Sethian 1988]:

$$\frac{\partial \phi}{\partial t} + (\vec{u} \cdot \nabla)\phi = 0, \qquad \frac{\partial \psi}{\partial t} + (\vec{u} \cdot \nabla)\psi = 0.$$

If $\rho_{IL}\, c_{IL}$ and $\rho_{IR}\, c_{IR}$ are assumed to be piecewise constant between each time step, Equation (2–5) can be approximated as

$$\begin{aligned} &\frac{p_I - p_{IL}}{\rho_{IL} c_{IL}} + (u_I - u_{IL}) = 0, \\ &\frac{p_I - p_{IR}}{\rho_{IR} c_{IR}} - (u_I - u_{IR}) = 0. \end{aligned}$$

Solving these for the interface pressure and normal velocity gives

$$u_I = \frac{p_{IL} - p_{IR} + \rho_{IL}u_{IL}c_{IL} + \rho_{IR}u_{IR}c_{IR}}{\rho_{IL}c_{IL} + \rho_{IR}c_{IR}},$$
$$p_I = \frac{p_{IL}\rho_{IR}c_{IR} + p_{IR}\rho_{IL}c_{IL} + (u_{IL} - u_{IR})\rho_{IL}c_{IL}\rho_{IR}c_{IR}}{\rho_{IL}c_{IL} + \rho_{IR}c_{IR}}, \tag{2–6}$$

where the values of $p_{IL}(p_{IR})$, $\rho_{IL}(\rho_{IR})$, $u_{Il}(u_{IR})$ and $c_{IL}(c_{IR})$ are taken from the left or right side of the interface in the normal direction.

It should be noted that tension waves are created due to suction from the cavity. The waves propagate in both the fluid and solid, which may lead to negative stresses in the vicinity of the fluid-structure interface and a subsequent (slight) negative p_{IR} or negative p_I due to numerical inaccuracy. However, if cavitation occurs near the fluid-solid interface, the acoustic impedance ($\rho_{IL}c_{IL}$) on the liquid side is negligible compared to ($\rho_{IR}c_{IR}$) on the solid side because the pressure and sound speed are (extremely) low in the cavitation region. As a result, $\rho_{IR}c_{IR} \gg \rho_{IL}c_{IL}$. Thus, Equation (2–6) can be simplified as follows:

$$u_I = u_{IR},$$
$$p_I = p_{IL} + [u_{IL} - u_{IR}]\rho_{IL}c_{IL}.$$

Here, the second member avoids the numerical prediction of a negative interface pressure when cavitation occurs near the fluid-solid interface.

3. Results and discussions

3.1. ***One-dimensional validation studies.*** First, two one-dimensional shock tube cases are computed to validate the current method for fluid-structure problems associated with shock impact on a structure. For the shock tube problem, there is an analytical solution derived from the Riemann problem [Toro 1997], which can be used to validate numerical methods for multiphase compressible flows. Both cases involve water-solid two-phase flows, where the high pressure lies in the water side (left). The computational domain is [0.0 m, 1.0 m] distributed uniformly with 200 grid points, the CFL number is 0.9, and the interface is initially at 0.4 m. The initial conditions for these two cases are:

Case 1: $u_l = 10\,\text{m/s}$, $p_l = 2000\,\text{bar}$, $u_r = 0\,\text{m/s}$, $p_r = 1\,\text{bar}$, $\rho_r = 7800\,\text{kg/m}^3$,

Case 2: $u_l = 50\,\text{m/s}$, $p_l = 25000\,\text{bar}$, $u_r = -5\,\text{m/s}$, $p_r = 25\,\text{bar}$, $\rho_r = 7.800088\,\text{kg/m}^3$.

Case 1. A water stream impinges onto a stationary solid, leading to shock wave propagation within the water and the solid. The computation is run to a final time of 5.0×10^{-3} s. Figure 1 shows pressure profiles calculated by the multiphase model and by the analytical model. The multiphase model's predictions compare well with the analytical solutions, and it captures accurately both shock waves within the water and the solid.

Case 2. Unlike Case 1, where the solid is initially stationary, Case 2 investigates what happens when the solid is already moving toward the water. The solution gives a shock wave in both water and solid. The computation is to run to a final time of 5.0×10^{-3} s. The strong impact leads to two strong shock

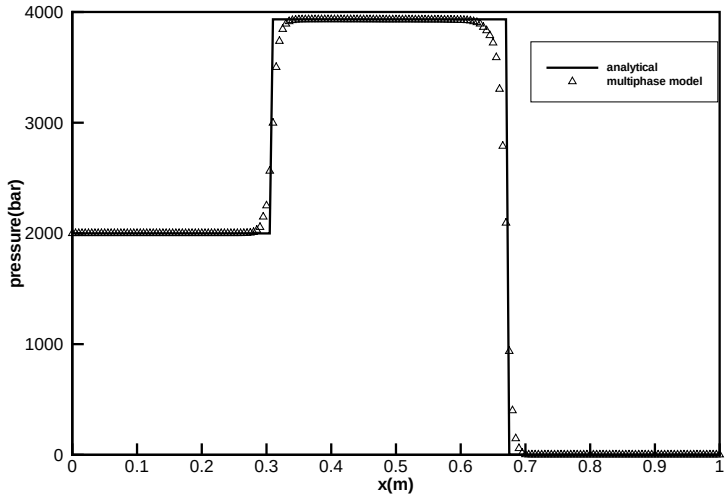

Figure 1. Pressure profiles for shock impact on structural boundary (case 1), where a right-moving ($u = 10$ m/s) water stream hits a stationary solid.

waves propagating at a high speed. The pressure profile produced by the multiphase model is in excellent agreement with the analytical solution, as shown in Figure 2.

3.2. ***Two-dimensional applications.*** The two-dimensional problem's configuration is shown in Figure 3. The shock waves, generated from the left boundary, hits a gas bubble with an initial radius of 0.5 m, leading to the collapse of the gas bubble. To investigate the effect of structural compressibility on the fluid and structural responses, the boundary is studied both as rigid and as compressible. The computational domain is $x \times y \in [-2, 2] \times [-4, 4]$ for the rigid case and $x \times y \in [-2, 6] \times [-4, 4]$ for the aluminum

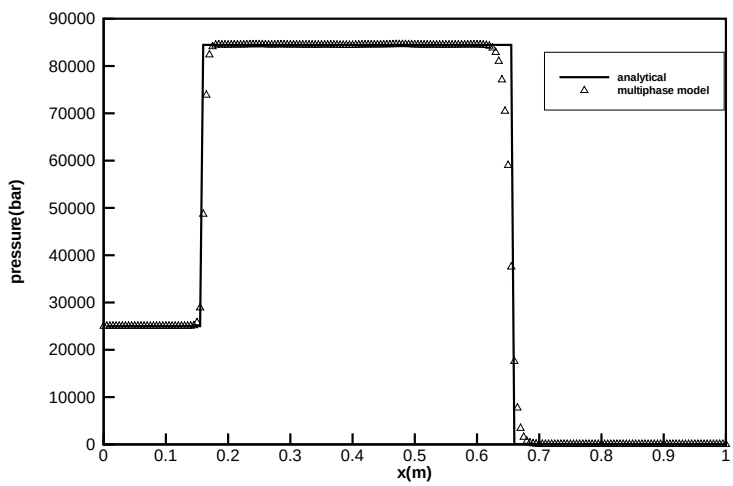

Figure 2. Pressure profiles for strong shock impact on structural boundary (case 2), where a right-moving ($u = 50$ m/s) water stream hits a left-moving solid ($u = -5$ m/s).

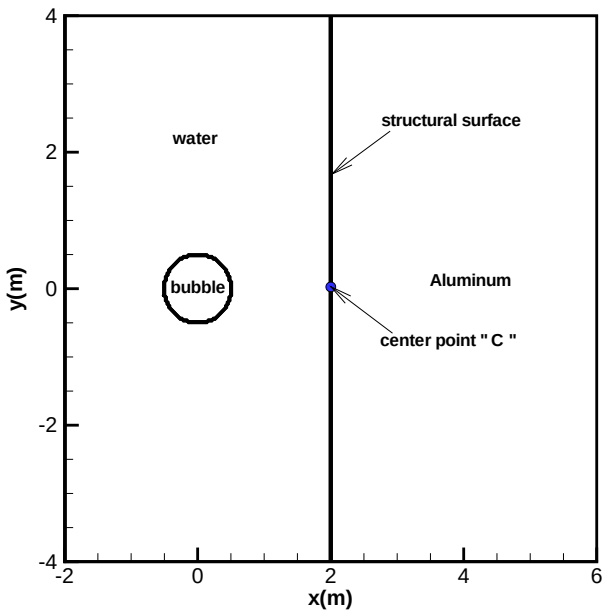

Figure 3. Schematic diagram for computations.

case, where the water-aluminum interface is at $y = 2m$. Uniform grids of size 160×320 and 320×320 (with $\Delta x = \Delta y = 1/40$ m) are placed in the computational domain for the rigid and aluminum case, respectively. Nonreflective boundary conditions are used for all four boundaries because the structure is considered to be semiinfinite. The initial conditions for two-dimensional computations are:

(i) Shock waves: $p = p_{\max} \exp(-t/t_{\text{decay}})$, $p_{\max} = 20000$ bar, $t_{\text{decay}} = 0.4$ ms.

(ii) Shock waves: gas bubble: $\rho_g = 1.0\,\text{kg/m}^3$, $p_g = 1.0$ bar, $u_g = 0.0$ m/s, $v_g = 0.0$ m/s, $\gamma_g = 1.4$.

(iii) Shock waves: water: $\rho_l = 1000\,\text{kg/m}^3$, $p_l = 1.0$ bar, $u_1 = 0.0$ m/s, $v_1 = 0.0$ m/s, $\gamma_l = 7.0$.

(iv) Shock waves: aluminum: $\rho_s = 2700\,\text{kg/m}^3$, $p_s = 1.0$ bar, $u_s = 0.0$ m/s and $v_s = 0.0$ m/s.

For two-dimensional computations, the CFL number is set to 0.45. To ensure the stability of computation, the time step is constrained by

$$\Delta t_f = \text{CFL} \frac{\min(\Delta x, \Delta y)}{\max\limits_{i,j}(|u_{i,j}| + |v_{i,j}| + c_{i,j})}, \tag{3–1}$$

where Δx and Δy are step sizes for x and y directions, and $u_{i,j}$, $v_{i,j}$, and $c_{i,j}$ are the flow velocity along the x-direction, the flow velocity along y-direction, and the flow sound speed.

To investigate the convergence of the current method for multidimensional applications, a grid resolution study is conducted. A series of uniform grids, 161×161 (with $\Delta x = \Delta y = 1/20$ m), 241×241 (with $\Delta x = \Delta y = 1/30$ m), and 321×321 (with $\Delta x = \Delta y = 1/40$m), are employed. The pressure-time history at the center C of the aluminum boundary surface C is shown in Figure 4a, and the corresponding pressure profiles along $y = 0$ at $t = 2.40$ ms are shown in Figure 4b. The two-dimensional computations converge well.

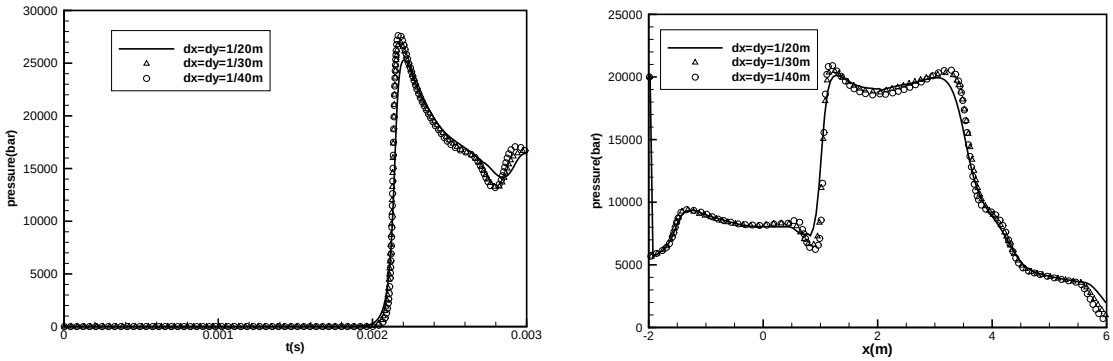

Figure 4. Convergence analysis: (a) pressure time histories at the center C of the structural surface; (b) pressure profiles along $y = 0$ at $t = 2.40$ ms (aluminum).

The remainder of this section contains an investigation of the collapse of a gas bubble near a semiinfinite rigid boundary and near an aluminum boundary.

First, a time series of pressure contours and velocity vectors are shown in Figure 5a through Figure 6b for the rigid boundary case. At time 1.20 ms (Figure 5a), the shock waves generated from the left boundary impact compress the left surface of the gas bubble, leading to a nonspherical bubble. The shock-bubble interaction creates rarefaction waves propagating spherically away from the bubble. At $t = 1.50$ ms (Figure 5b), the gas bubble has been compressed, and a toroidal bubble is formed. The velocity vectors point towards the right side of the rigid boundary due to low pressure inside. At $t = 1.65$ ms (Figure 5c), the cavitation bubble is near collapse. Large velocity gradients develop around the right bubble interface, pointing towards the rigid boundary. The cavitation bubble collapses after $t = 1.80$ ms (Figure 5d), resulting in a high-speed, high-pressure shock wave that propagates spherically outward. At this time, the initial shock waves from the left boundary approach the rigid solid boundary. At time 2.10 ms (Figure 6a), the shock wave generated from the bubble collapse has almost reached the rigid boundary, while the initial shock waves have already impacted and reflected from it, except at the region near its center. Obviously, the gas bubble itself will cushion the center, reducing the initial shock loading. Figure 6a and Figure 6b show that two tiny bubbles are created after the original large bubble collapses. In the model, the level set technique automatically changes the interface numbers (from one to two gas bubbles). At $t = 2.55$ ms (Figure 6b), the shock wave generated from the bubble's collapse has arrived at and reflected from the rigid boundary. A very high pressure region develops near the center region of the rigid boundary, because the reflected shock wave merges with the new shock wave generated by the collapse of the gas bubble.

The peak flow velocity appears near $x = 0.0$ m at $t = 1.25$ ms, because the low bubble pressure allows the flow to move into it at a higher velocity. The flow velocity decreases when the bubble is compressed as the internal pressure increases and because rarefaction waves propagate against the flow. After $t = 1.25$ ms, the flow velocity starts to decrease as energy dissipates into the surrounding fluid and as the flow interacts with shock waves reflecting from the solid boundary ($t = 2.25$ ms and 2.70 ms). To illustrate shock loading on the rigid boundary, pressure distributions along the rigid boundary at different

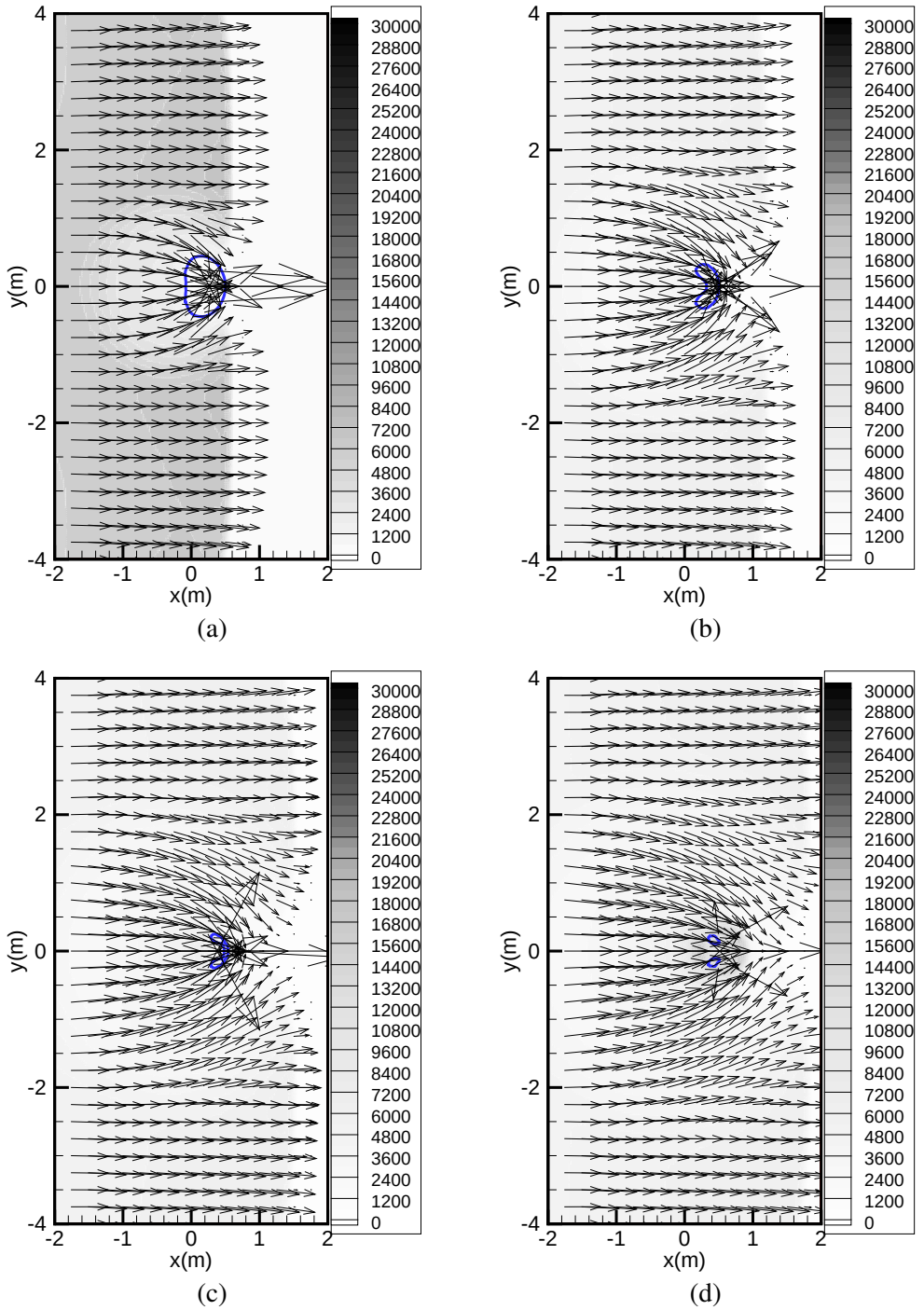

Figure 5. Pressure contours and velocity vectors for bubble collapse near a rigid boundary: (a) $t = 1.20$ ms, (b) $t = 1.50$ ms, (c) $t = 1.65$ ms, (d) $t = 1.80$ ms.

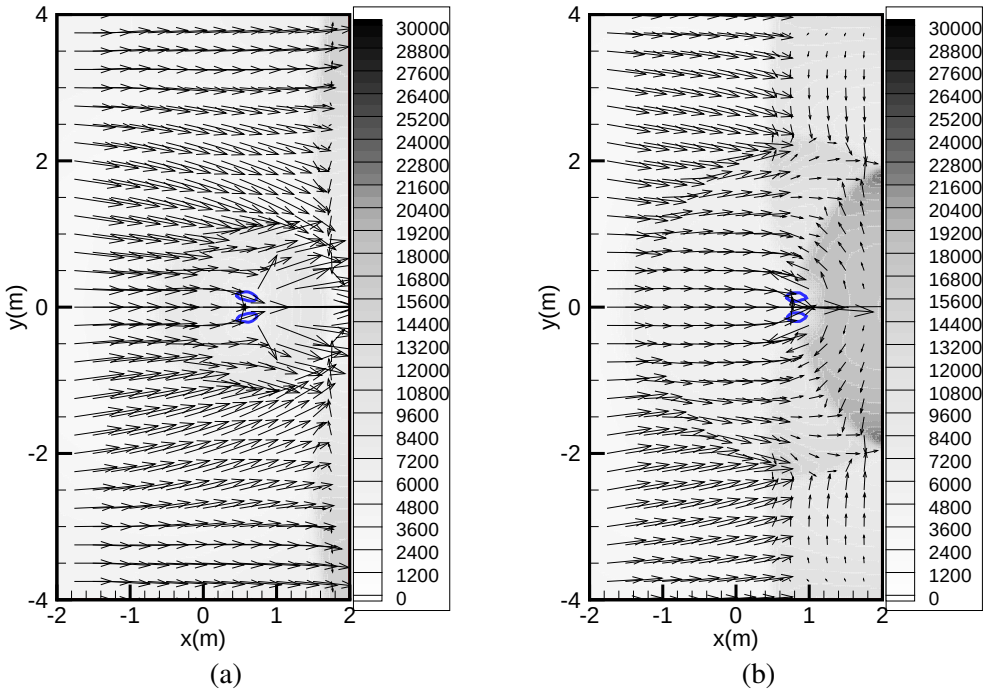

Figure 6. Later pressure contours and velocity vectors for bubble collapse near a rigid boundary: (a) $t = 2.10$ ms, (b) $t = 2.55$ ms.

times after the bubble collapse are shown in Figure 8. At $t = 1.95$ ms, the pressure pulse caused by the bubble

Figure 7 depicts a time series of velocity profiles along $y = 0$. collapse has not yet reached the rigid boundary, while the initial shock wave has already reflected from the rigid boundary. The presence of

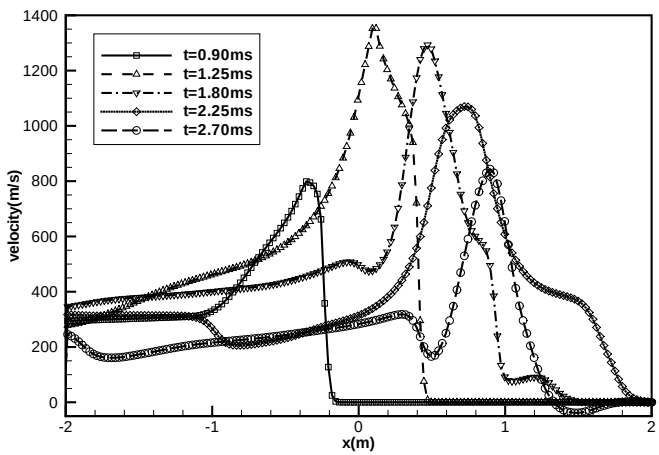

Figure 7. Velocity profiles along $y = 0$ (rigid boundary case).

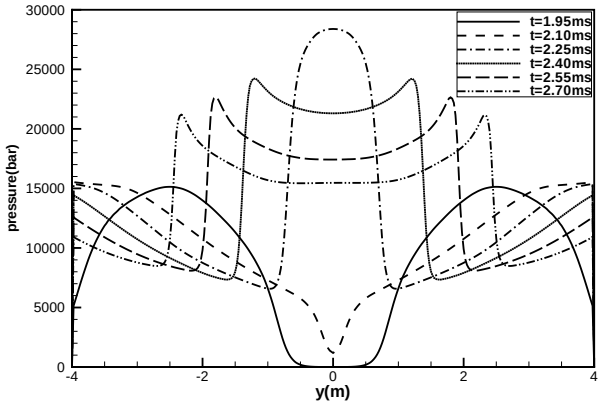

Figure 8. Pressure distributions along the structural surface (rigid boundary case).

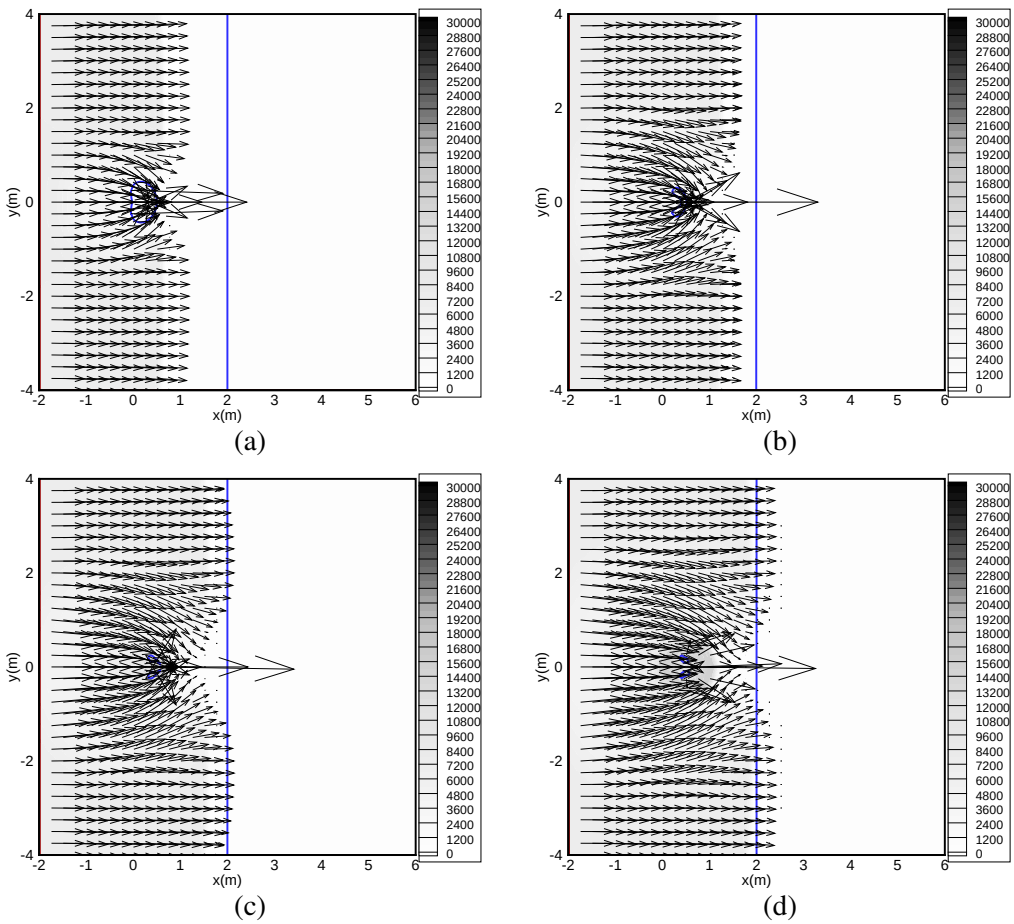

Figure 9. Pressure contours and velocity vectors for the aluminum boundary: (a) $t = 1.20$ ms, (b) $t = 1.50$ ms, (c) $t = 1.65$ ms, (d) $t = 1.80$ ms.

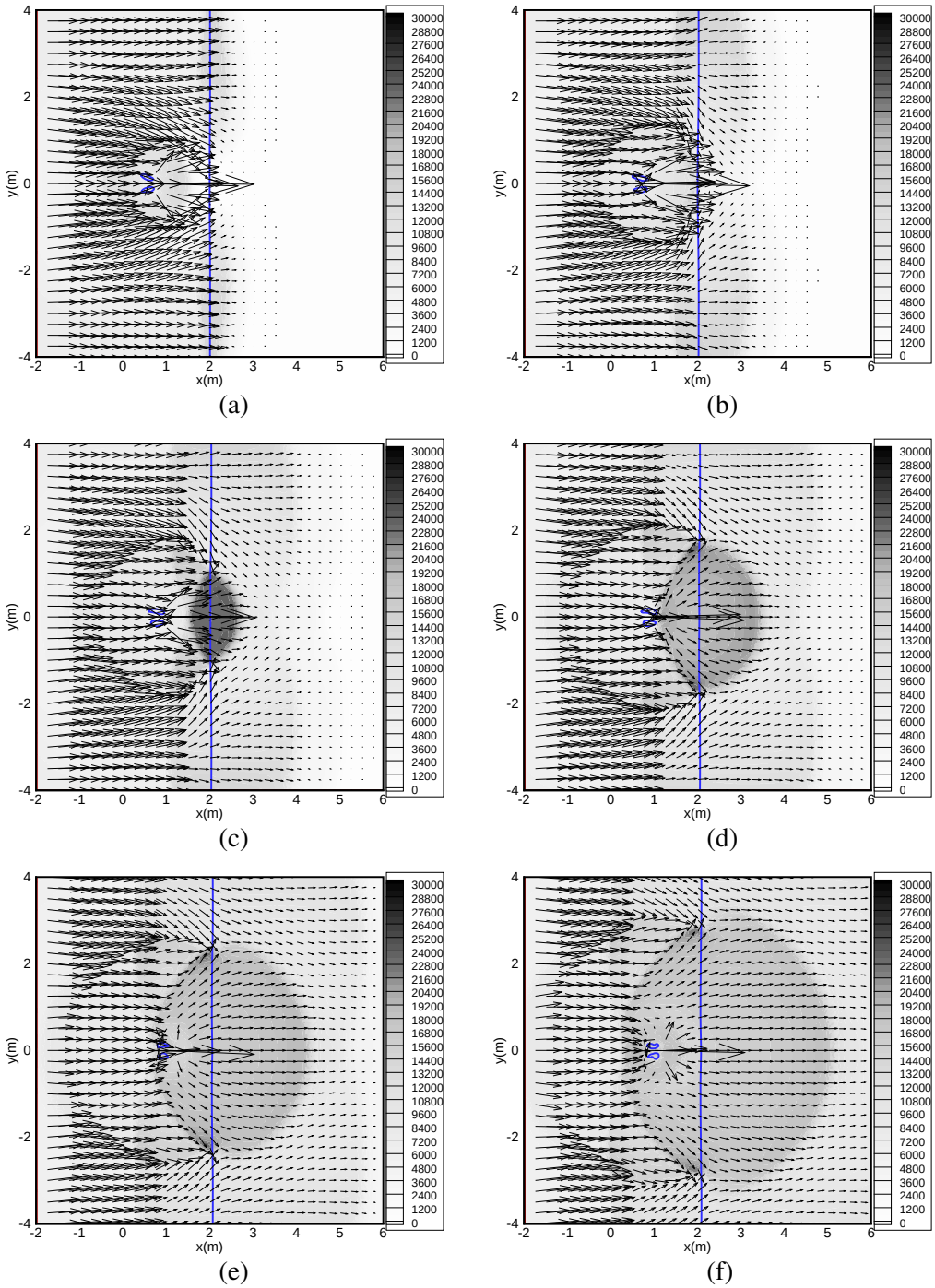

Figure 10. Later pressure contours and velocity vectors for the aluminum boundary: (a) $t = 1.95$ ms, (b) $t = 2.10$ ms, (c) $t = 2.25$ ms, (d) $t = 2.40$ ms, (e) $t = 2.55$ ms, (f) $t = 2.70$ ms.

the bubble maintains atmospheric pressure near the center, but the pressure away from there is very high due to the initial shock wave. The pressure pulse reaches the solid boundary at around $t = 2.10$ ms. Thus, the pressure at the center region of the solid boundary starts to increase and reaches its highest value at $t = 2.25$ ms as the secondary shock generated from the bubble collapse arrives. After that, the pressure here decreases due to interaction between the initial shock wave and the rarefaction waves reflected from the solid and bubble boundaries (from $t = 2.25$ ms to $t = 2.70$ ms).

For the semiinfinite solid body made of aluminum, the flow physics is similar to the rigid boundary case before the shock waves impact on the boundary (see Figure 9a). The fluid-solid boundary is shown as a vertical solid line. When the initial shock wave hits the aluminum boundary at $t = 1.95$ ms, the shock wave both reflects from it and propagates through it (see Figure 10a). When the shock wave caused by bubble collapse reaches the boundary, the velocity is particularly high at the center region, leading to the structural deformation and shock propagation through the center (Figure 10). The shock wave generated from the bubble collapse propagates throughout the structural domain and can lead to significant stress within the structure. The deformation of the aluminum boundary away from the center can be observed in Figure 10e and Figure 11. More displacement occurs away from the center ($y = 0$) for $t \leq 2.1$ ms due to the air cushioning effect provided by the collapsing bubble. For $t > 2.1$ ms, more displacement occurs at the center due to the highly focused pressure reload created by the collapse.

To examine the fluid and structural response, the fluid pressure p contours (lines) and the normalized solid deviator stress $2s/Y$ contours (flooded) are plotted together at times 1.80 ms, 1.95 ms, 2.10 ms, and 2.25ms in Figure 12. $|2s/Y| = 1$ implies the material has yielded and is in the strain hardening regime. Beginning at the initial shock wave impact on the solid boundary at $t = 1.80$ ms (Figure 12a), the normalized solid deviator stress increases with time, and, at $t = 1.95s$ ms, the aluminum material begins

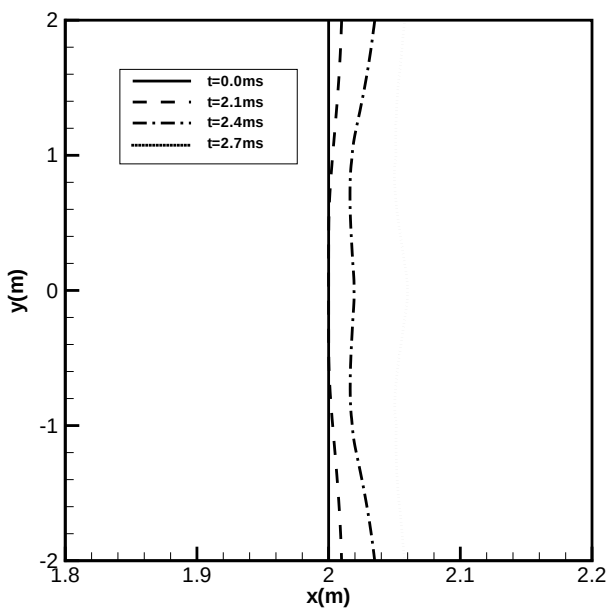

Figure 11. The progressive deformation of the aluminum boundary.

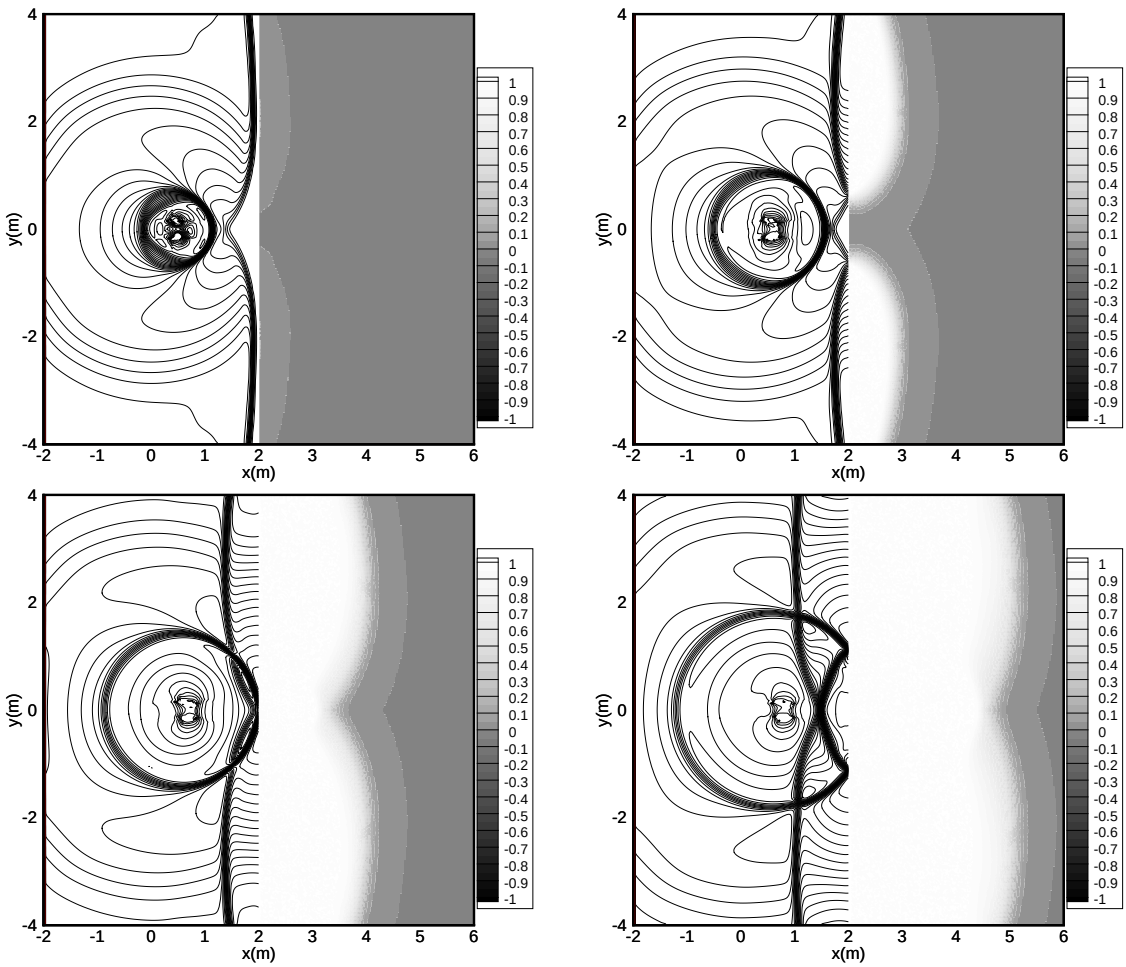

Figure 12. Fluid pressure contours (lines) and $2s/Y$ normalized deviator stress contours (flood) for the aluminum boundary: (a) $t = 1.80$ ms, (b) $t = 1.95$ ms, (c) $t = 2.10$ s, (d) $t = 2.25$ ms.

to experience plastic deformation, except at the center (see Figure 12b) because of the aforementioned cushioning. At $t = 2.10$ ms, the shock wave generated from the bubble collapse hits the boundary, leading to plastic deformation at the center (Figure 12c). The entire solid region almost yields at $t = 2.25$ ms due to the combined initial shock loading and gas bubble reloading (Figure 12d). It can be concluded that a gas bubble near the structural surface first helps to reduce the shock load, but then generates a strong focused secondary reload when it collapses.

The velocity profiles along $y = 0$ for a series of times are provided in Figure 13 to exhibit the time varying flow variables, which are similar to the rigid boundary case. It should be noted that the center of the structural surface moves during the pressure reload from the bubble collapse. This can be seen at $t = 2.40$ ms and $t = 2.70$ ms in Figure 11. In addition, the pressure distributions along the surface are shown in Figure 14 to illustrate the pressure loading of the aluminum boundary. The pressure peaks at

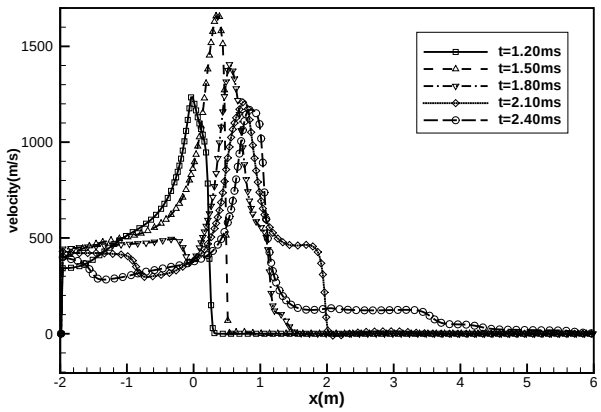

Figure 13. Velocity profiles along $y = 0$ (aluminum boundary case).

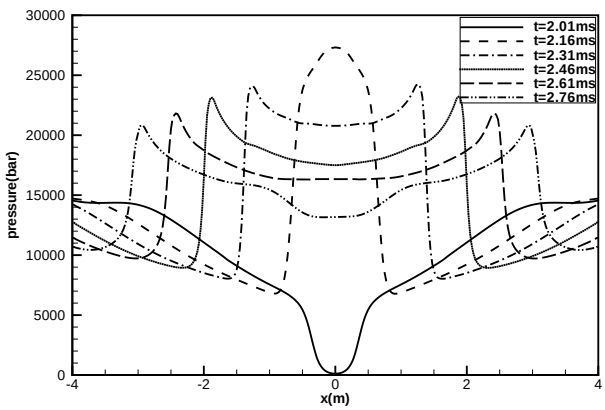

Figure 14. Pressure distributions along structural surface (aluminum boundary case).

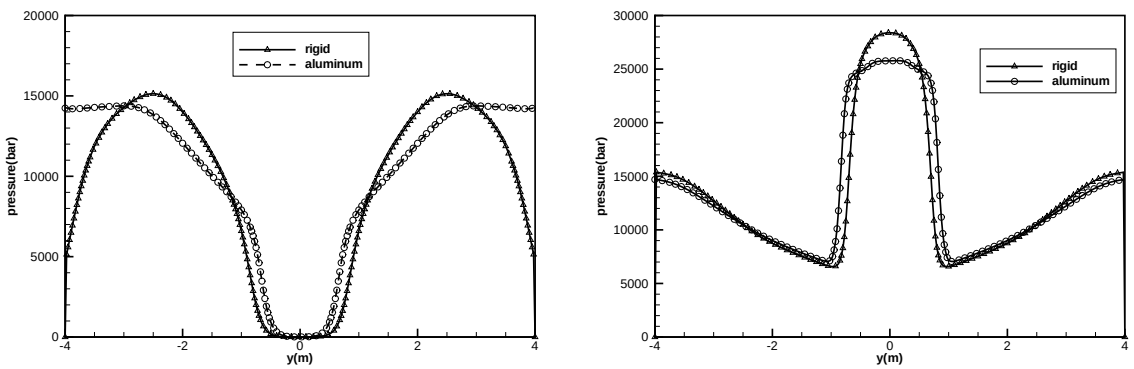

Figure 15. Comparison of pressure distributions along structural surface for the rigid case and the aluminum case: (a) before gas bubble reload at $t = 1.95$ ms, (b) after gas bubble reload at $t = 2.25$ ms.

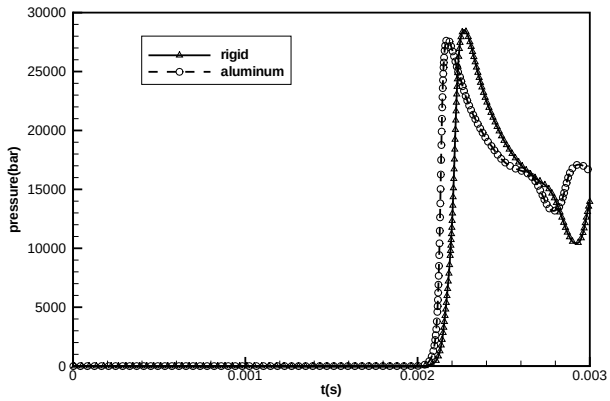

Figure 16. Comparison of pressure histories at the center C for both the rigid and the aluminum boundary.

$t = 2.16$ ms for the center point C as it experiences the pressure loading created by the bubble collapse. In addition, pressure distributions along the rigid boundary and the aluminum boundary before the gas bubble reload at $t = 1.95$ ms, and after gas bubble reload at $t = 2.25$ ms, are shown in Figure 15a and 15b for comparison. Figure 15a shows that pressures away from the gas bubble for the rigid case are higher than for the aluminum case, because energy dissipates in the deformable aluminum. The pressure distributions near the bottom/top regions of the structural surface (left and right regions in Figure 15a) are different for the rigid and the aluminum cases, again mainly because of shock energy dissipates through solid deformation.

The shock reflects more weakly from the aluminum surface than from the rigid surface, because of the fully reflective boundary condition. Due to the strong reflected shock from the rigid surface, the pressure near the rigid boundary drops more rapidly than it does near the aluminum, leading to a lower predicted pressure distribution near the bottom and top regions of the structural surface. After the bubble collapse, Figure 15b shows that the peak pressure at the center due to gas bubble reload for the rigid case is higher than for the aluminum case. This is once again due to the energy dissipation through the aluminum material.

The pressure histories at the center C are recorded and compared for the rigid and aluminum cases. Figure 16 shows that the initial shock wave arrives at the boundary at approximately the same time but the rate of pressure increase and the peak interface pressure for rigid and aluminum boundaries are different. The peak pressure is higher for the rigid boundary because it does not dissipate energy. However, the rate of pressure increase is lower for the rigid boundary due to interaction between the initial shock wave and the reflected rarefaction wave. The differences between the rigid and aluminum boundaries are not significant due to the relatively high elastic modulus of aluminum and due to the short load duration, both of which limit the energy dissipated through deformation.

To understand the influence of the bubble on the interface pressure, the pressure history at the center C is compared with and without the gas bubble in Figure 17. The results indicate that the initial shock wave arrives at the boundary much later when there is a gas bubble than when there is not, due to the air cushioning effect. However, when the bubble is forced to implode from high shock load, the peak

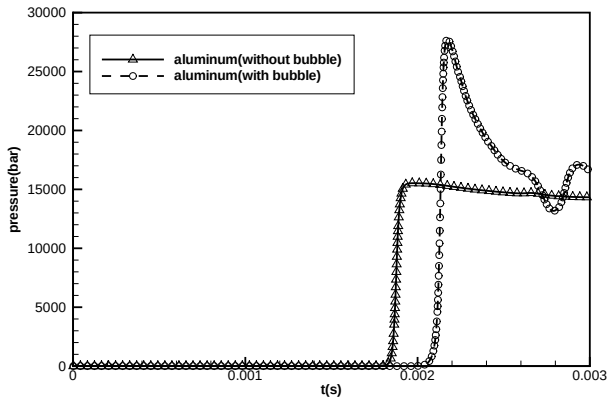

Figure 17. Comparison of pressure histories at center point C for the aluminum boundary with and without the gas bubble.

pressure caused by the collapse and the delayed shock impact are both much higher than the peak pressure caused by the initial shock wave without the bubble. Thus, it is important to consider the effect of gas bubbles for the overall assessment of structural response to a high intensity shock load.

4. Concluding remarks

A multiphase compressible hydrodynamic model was applied to study multidimensional shock-bubble-structure interactions. In particular, the shock-induced collapse of a gas bubble near a planar compressible solid wall has been investigated. A toroidal collapse of gas bubble and a strong shock generated from bubble collapse have been observed. During the bubble collapse, a high-velocity, high-pressure, jet-like fluid flow hits the center region of the boundary. The collapse is so violent that the pressure impulse release rivals the initial shock wave. The deformation of aluminum boundary is due to the initial shock loading and the subsequent shock-induced collapse of the bubble. It is found that a gas bubble near the center of the structural surface helps to reduce initial shock loading there but then causes a stronger shock reload due to the high intensity microjet created as it collapses. In addition, the gas-water and water-solid interfaces are well represented, the change in the number of interfaces is captured automatically, and symmetric flow fields are obtained. It should be noted that the current model has some severe limitations. The hydro-elasto-plastic (HEP) model assumes the deviatoric stress to be secondary, but this is only reasonable when the structure is under strong impact normal to the planar solid surface; the HEP ignores the shear (s-type) waves and assumes the pressure (p-type) waves travel along the principal directions, which limits its applicability to shock duration, strong shock loading normal to a homogeneous isotropic planar structure. The current Eulerian fluid/Eulerian solid has been validated against the one-dimensional analytical solutions for the shock-tube problem, but additional experimental validation studies are needed, especially for the HEP equation of state. To simulate general fluid-structure interaction involving arbitrary shock loads on anisotropic or inhomogeneous mediums, the solid dynamics can be better captured using a Lagrangian-FEM solver where the solid behavior is described using the material stress-strain constitutive relationships. A one-dimensional Eulerian fluid/Lagrangian solid approach has been presented in [Xie et al. 2007a]. A two-dimensional extension of the Eulerian-Lagrangian solver is ongoing.

References

[Chahine et al. 2003] G. L. Chahine, K. M. Kalumuck, and C.-T. Hsiao, "Simulation of surface piercing body coupled response to underwater bubble dynamics utilizing 3DynaFS, a three-dimensional BEM code", *Comput. Mech.* **32** (2003), 319–326.

[Deshpande and Fleck 2005] V. S. Deshpande and N. A. Fleck, "One-dimensional shock response of sandwich beams", *J. Mech. Phys. Solids* **53** (2005), 23–47.

[Deshpande et al. 2006] V. S. Deshpande, A. Heaver, and N. A. Fleck, "An underwater shock simulator", *Proc. R. Soc. A* **462** (2006), 1021–1041.

[Houlston et al. 1985] R. Houlston, J. E. Slate, N. Pegg, and C. G. Desrochers, "On analysis of structural response of ship panels subjected to air blast loading", *Comput. Struct.* **21** (1985), 273–289.

[Kalumuck et al. 1995] K. M. Kalumuck, R. Duraiswami, and G. L. Chahine, "Bubble dynamics fluid-structure interaction simulation by coupling fluid BEM and Structural FEM codes", *J. Fluids. Struct.* **9** (1995), 861–883.

[Kambouchev et al. 2006] N. Kambouchev, L. Noels, and R. Radovitzky, "Nonlinear compressibility effects in fluid–structure interaction and their implications on the air-blast loading of structures", *J. Appl. Phys.* **100** (2006), 1–10.

[Knapp et al. 1970] R. P. Knapp, J. W. Daily, and F. G. Hammitt, *Cavitation*, McGraw-Hill, 1970.

[Lindau and Lauterborn 2003] O. Lindau and W. Lauterborn, "Cinematographic observation of the collapse and rebound of a laser-produced cavitation bubble near a wall", *J. Fluid Mech.* **479** (2003), 327–348.

[Liu et al. 2003] T. G. Liu, B. C. Khoo, and K. S. Yeo, "Ghost fluid method for strong shock impacting on material interface", *J. Comput. Phys.* **190** (2003), 651–681.

[McCoy and Sun 1997] R. W. McCoy and C. T. Sun, "Fluid-structure interaction analysis of a thick-section composite cylinder subjected to underwater blast loading", *Compos. Struct.* **31** (1997), 45–55.

[Ohl and Irink 2003] C. D. Ohl and R. Irink, "Shock-wave-induced jetting of micron-size bubbles", *Phys. Rev. Lett.* **90** (2003), 214502.

[Ohl and Wolfrum 2003] C. D. Ohl and B. Wolfrum, "Detachment and sonoporation of adherent HeLa-cells by shock wave-induced cavitation", *Biochim. Biophys. Acta* **1624** (2003), 131–138.

[Osher and Sethian 1988] S. Osher and J. A. Sethian, "Fronts propagating with curvature dependent speed. Algorithms based on Hamilton-Jacobi formulations", *J. Comput. Phys.* **79** (1988), 12–49.

[Philipp and Lauterborn 1998] A. Philipp and W. Lauterborn, "Cavitation erosion by single laser-produced bubbles", *J. Fluid Mech.* **361** (1998), 75–116.

[Tang and Sotiropoulos 1999] H. S. Tang and F. Sotiropoulos, "A second-order Godunov method for wave problems in coupled solid-water-gas systems", *J. Comput. Phys.* **151** (1999), 790–815.

[Tomita and Shima 1986] Y. Tomita and A. Shima, "Mechanisms of impulsive pressure generation and damage pit formation by bubble collapse", *J. Fluid Mech.* **169** (1986), 535–564.

[Tomita et al. 2002] Y. Tomita, P. B. Robinson, R. P. Tong, and J. R. Blake, "Growth and collapse of cavitation bubbles near a curved rigid boundary", *J. Fluid Mech.* **466** (2002), 259–283.

[Toro 1997] E. F. Toro, *Riemann solvers and numerical methods for fluid dynamics*, Springer Publication Company, 1997.

[Van Leer 1974] B. Van Leer, "Towards the ultimate conservative difference schemes II: Monotonicity and conservative combined in a second-order scheme", *J. Comput. Phys.* **14** (1974), 361–370.

[Vaziri and Hutchinson 2007] A. Vaziri and J. W. Hutchinson, "Metal sandwich plates subject to intense air shocks", *Int. J. Solids Struct.* **44** (2007), 2021–2035.

[Xie et al. 2006] W. F. Xie, Y. L. Young, and T. G. Liu, *Multiphase modeling of dynamic fluid-structure interaction during close-in explosion*, 2006. under review.

[Xie et al. 2007a] W. F. Xie, Z. K. Liu, and Y. L. Young, *An Eulerian-Lagrangian approach for fluid-structure interaction with large solid deformation and fluid cavitation*, 2007. Under review.

[Xie et al. 2007b] W. F. Xie, Y. L. Young, T. G. Liu, and B. C. Khoo, "Dynamic response of deformable structures subjected to shock load and cavitation reload", *Comput. Mech.* **40** (2007), 667–681.

[Xue and Hutchinson 2004] Z. Xue and J. W. Hutchinson, "A comparative study of blast-resistant metal sandwich plates", *Int. J. Impact Eng.* **30** (2004), 1283–1305.

[Zhong et al. 1997] P. Zhong, F. H. Cocks, I. Cioanta, and G. M. Preminger, "Controlled, forced collapse of cavitation bubbles for improved stone fragmentation during shock wave lithotripsy", *J. Urology* **158** (1997), 2323–2328.

Received 18 May 2007. Accepted 23 May 2007.

WENFENG XIE: wxie@princeton.edu
Dept of Civil and Environmental Engineering, E-228, EQUAD, Princeton University, Princeton, New Jersey 08544, United States

YIN LU YOUNG: yyoung@princeton.edu
Dept of Civil and Environmental Engineering, E-326, EQUAD, Princeton University, Princeton, New Jersey 08544, United States